Complex manifold of Rashba and image-potential states on Bi/Ag(111)

Philipp Rosenzweig, Sebastian Otto, and Thomas Fauster
Lehrstuhl für Festkörperphysik, Friedrich-Alexander-Universität Erlangen-Nürnberg, 91058 Erlangen, Germany

(Received 17 May 2018; revised manuscript received 7 August 2018; published 24 August 2018)

Angle-resolved, mono- and bichromatic two-photon photoemission was used to study the electronic structure at the surface of the giant Rashba system Bi/Ag(111). The photoemission intensity maps are exceptionally rich in structure due to a large manifold of initial and intermediate states that allow for various resonant interband transitions. Using different photon energies, we succeeded in disentangling the complex experimental data. Close to the Fermi level the unoccupied, Rashba-split $p_x p_y$ ($m_j = 1/2$) surface state can be identified with a Rashba parameter of 3.0 ± 0.2 eV Å and a lifetime of 26 ± 5 fs. At higher energies the spin-split $p_x p_y$ ($m_j = 3/2$) and p_z bands as well as the first three members of a series of image-potential resonances were observed. Circular dichroism was used to gain information on the spin structure of both the initial and intermediate states and to corroborate the assignment to Rashba bands.

DOI: 10.1103/PhysRevB.98.085430

I. INTRODUCTION

The coupling between electron momentum and the orientation of electron spin has received considerable attention in recent years because it opens the field for practical application of spintronic devices [1]. In topological insulators the locking of momentum and spin is guaranteed by topology [2]. The broken symmetry at interfaces of materials with large spin-orbit coupling also couples momentum and spin, resulting in a spin-split electronic structure. This well-known Rashba effect [3,4] is particularly pronounced for systems with a large potential gradient at the interface [5–7]. The prototypical system with a giant Rashba-type spin splitting is Bi/Ag(111) [5], which has been studied extensively with various techniques [8–13].

One third of a monolayer of bismuth on Ag(111) forms a $BiAg_2$ substitutional surface alloy with a $(\sqrt{3} \times \sqrt{3})R30^\circ$ periodicity in the top layer [9]. Its surface electronic structure is plotted schematically in Fig. 1(a). The occupied sp_z bands are split into two branches shifted away from $\overline{\Gamma}$ in parallel momentum by k_R. From the energy difference E_R between the crossing point and the band extrema the Rashba parameter $\alpha_R = 2E_R/k_R$ can be obtained, which has a value of 3.05 eV Å for Bi/Ag(111) [5]. The $p_x p_y$ ($m_j = 1/2$) bands also show Rashba-type spin splitting. They have been observed by spin-polarized inverse photoemission [12] and scanning tunneling spectroscopy [10] above the Fermi level E_F and by angle-resolved photoemission below the Fermi level [13,14]. Inverse photoemission has a limited resolution, and no value for the Rashba parameter was given in Ref. [12]. The unoccupied electronic structure offers further bands, $p_x p_y$ ($m_j = 3/2$) and p_z, in the band gap of the projected bulk band structure, as well as a series of image-potential states (IPSs) [15,16] just below the vacuum level E_{vac}. The $p_x p_y$ ($m_j = 3/2$) and p_z bands were found in calculations and identified in inverse photoemission [8,12]. Note that while the two-dimensional sp_z, $p_x p_y$, and p_z surface bands are all intrinsic to the $BiAg_2$ surface alloy, the Shockley surface state of Ag(111) is quenched [17]. However, surface alloying does not affect the bulk bands of the underlying Ag substrate, which have to be clearly delimited from the alloy-induced surface states discussed above.

Two-photon photoemission (2PPE) [15] is the method of choice to study unoccupied electronic surface states. In addition to a superior resolution compared to inverse photoemission it may provide information on the lifetimes of the observed states. The polarization may be changed easily, and information about the spin structure can be obtained using circular dichroism [7]. In this work we study the unoccupied electronic states of Bi/Ag(111) using angle-resolved two-photon photoemission. All bands sketched in Fig. 1(a) are observed and agree well with the available calculations [8,12]. The large manifold of occupied and unoccupied states allows for many resonant interband transitions, as indicated by the arrows in Fig. 1(a). The associated complexity of the two-photon photoemission results and their analysis is a significant step beyond previous studies. Circular dichroism is used to obtain information on the spin structure of the observed states and to confirm the assignment to Rashba bands.

II. EXPERIMENT

All experiments were performed in ultrahigh vacuum at a base pressure and temperature of 3×10^{-10} mbar and 90 K, respectively. Angle-resolved photoelectron spectroscopy was carried out using either the second harmonic (monochromatic two-photon photoemission, $2h\nu = 3.02$–3.26 eV), the fundamental and third harmonics (bichromatic two-photon photoemission, $1h\nu = 1.51$–1.63 eV and $3h\nu = 4.54$–4.89 eV), or the fourth harmonic [one-photon photoemission (1PPE), $4h\nu = 6.20$ eV] of a Ti:sapphire oscillator with a repetition rate of 90 MHz. The second harmonic $2h\nu$ is generated by frequency doubling of the fundamental $1h\nu$ in a lithium triborate crystal, while β-barium borate crystals provide the third, $3h\nu = 1h\nu + 2h\nu$, and fourth, $4h\nu = 1h\nu + 3h\nu$, harmonics via sum-frequency generation. The light was p polarized and incident in the $\overline{\Gamma K}$ mirror plane (for normal photoelectron

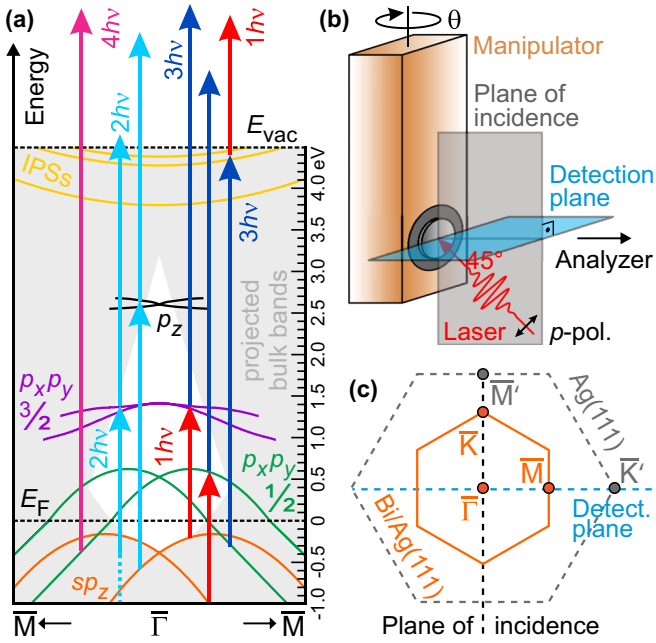

FIG. 1. (a) Schematic band structure of Bi/Ag(111) with relevant one- and two-photon photoemission transitions. (b) Experimental geometry of light incidence and electron detection. (c) Surface Brillouin zones of the Ag(111) substrate (gray dashed lines) and the $(\sqrt{3} \times \sqrt{3})R30^\circ$ reconstructed Bi/Ag(111) surface (orange lines).

emission), at an angle of 45° with respect to the surface normal [see Figs. 1(b) and 1(c)]. The emission angle Θ was controlled by rotating the sample around its vertical axis. Spectra were recorded in the $\overline{\Gamma M}$ direction with a hemispherical analyzer (Omicron EA300HR with seven channeltrons) at a constant energy resolution of 34 meV and an angular resolution of ±0.8°.

For the circular dichroism (CD) measurements, spectra were taken for right- and left-circularly polarized light. The difference of these spectra normalized to the sum directly gives the dichroism signal. Note that the sum of the spectra might differ from the corresponding spectra obtained with *p*-polarized light due to the *s*-polarized components in the circularly polarized light.

The Ag(111) single crystal was cleaned by multiple successive sputtering-annealing cycles. The quality of the substrate was assessed by monitoring the low-energy electron diffraction pattern as well as the Shockley surface state and image-potential states in one- and two-photon photoemission, respectively. The long-range ordered $(\sqrt{3} \times \sqrt{3})R30^\circ$ Bi/Ag(111) substitutional surface alloy was reliably prepared by evaporating 1/3 of a monolayer of Bi from a home-built Knudsen-cell-type evaporator (at a rate of 0.13 monolayer/min) onto the Ag substrate (held at room temperature) followed by annealing to 220 °C for 2 min.

The work function of Bi/Ag(111) is determined from the low-energy cutoff of monochromatic two-photon photoemission spectra at normal emission to 4.49 ± 0.01 eV. This value is smaller than the lowest accessible photon energy $3h\nu = 4.54$ eV of the frequency-tripled laser pulses. Therefore, bichromatic measurements were performed at a bias voltage of −0.5 V between the sample and the analyzer such that the difference in work function of the analyzer lens system (around 5.2 eV) and the sample is not fully compensated for and the corresponding retarding electric field effectively suppresses the $3h\nu$-associated, direct photoemission intensity. To allow for a better comparison with bichromatic two-photon photoemission data, the one-photon photoemission patterns shown in this paper were recorded at the same bias voltage of −0.5 V. For the monochromatic two-photon photoemission measurements, a bias voltage of −4.5 V corresponding to an accelerating electric field between the sample and the analyzer was applied, and the angular distributions were corrected following Ref. [18].

III. RESULTS

The large manifold of occupied and unoccupied bands shown in Fig. 1(a) with many resonant interband transitions poses a challenge to the analysis of the two-photon photoemission data. The presentation of the results therefore starts with the initial states seen in the one-photon photoemission spectra. The $p_x p_y$ ($m_j = 1/2$) bands extend above the Fermi level where they are picked up by bichromatic two-photon photoemission pumped by the first harmonic. The higher $m_j = 3/2$ bands are reached as intermediate states by monochromatic two-photon photoemission using the second harmonic and bichromatic two-photon photoemission probed by the third harmonic. Strong signals for the image-potential resonances are obtained in bichromatic two-photon photoemission probed by the first harmonic. The section closes with the presentation of the circular dichroism data that are discussed in view of the various spin-split and image-potential bands.

A. $m_j = 1/2$ bands near E_F

The bottom part of Fig. 2 shows photoemission data of the occupied band structure taken with 6.20 eV photon energy. The bright emission close to the lower edge of the data range marked by the dashed gray guide to the eye is assigned to a bulk transition and is observed also on the clean Ag(111) surface. It is attributed to direct optical transitions between free-electron-like bulk bands [19,20]. The two downward-dispersing, parabolic bands crossing at −0.36 ± 0.02 eV (indicated by the dashed orange guides to the eye) agree well with previous measurements and are assigned to the occupied, spin-split sp_z bands [8]. From the spectra in our studies the Rashba parameter is obtained as 3.04 ± 0.08 eV Å, in perfect agreement with previous work [5,13].

Several weaker, downward-dispersing branches are also observed and are marked by the linear, dashed green guides to the eye. They are assigned to the $p_x p_y$ ($m_j = 1/2$) bands. All these bands show higher intensity inside the band gap of the projected bulk band structure [13], where they have proper surface-state character. The dispersion of the occupied $p_x p_y$ bands below E_F is difficult to extract from the data because of the low intensity and the overlap with the sp_z bands. However, the Fermi level crossings are obtained reliably from the corresponding momentum distribution curve [5] and are marked by green circles in Fig. 2. The $p_x p_y$ bands above E_F can be found by bichromatic two-photon photoemission using the fundamental as pump and the third harmonic as probe

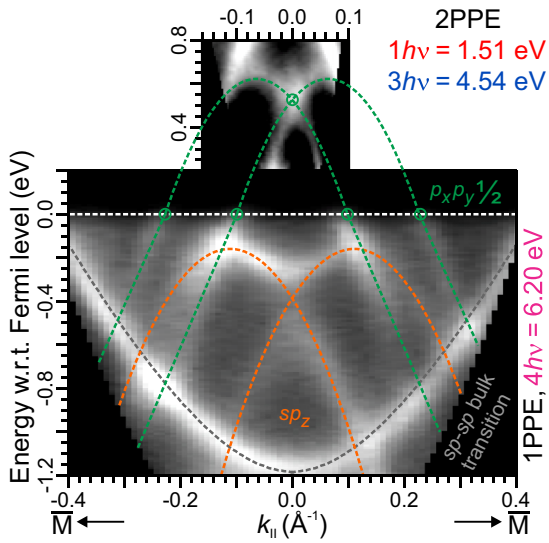

FIG. 2. Photoemission data of the occupied band structure taken with 6.20 eV photon energy complemented by two-photon photoemission data for the unoccupied states pumped by 1.51 eV and probed by 4.54 eV photon energy. Dashed orange and green curves indicate the sp_z and $p_x p_y$ bands derived from the experimental data (see text for details). The gray dashed guide to the eye marks the dispersion of a direct transition between bulk bands.

photons. The corresponding data are shown in the top part of Fig. 2. The crossing of the two Rashba bands at 0.53 ± 0.02 eV above the Fermi level and their inner, downward-dispersing branches are clearly seen. Note that the energetic shift of these spectral features corresponds exactly to the change in photon energy of the third harmonic (see Fig. 6 below), which corroborates their energetic position close to E_F. The high intensity above the Rashba bands at parallel momentum $k_\parallel = \pm 0.08$ Å^{-1} is due to initial states and will be discussed in Sec. III B. The energy of the branch crossing at $k_\parallel = 0$ and the Fermi level crossings are used to obtain the Rashba parameter of the $p_x p_y$ bands to 3.0 ± 0.2 eV Å, assuming a parabolic dispersion in the energy range above the Fermi level. The dashed green curves represent the corresponding fit of the Rashba model. This assumption, as well as the resulting value for the Rashba parameter, is well supported by the band structure calculations [8,12].

From the corresponding time-resolved two-photon photoemission measurements, the lifetime of the spin-split $p_x p_y$ ($m_j = 1/2$) state is extracted as 26 ± 5 fs based on a simplified model that allows for an analytical solution to the optical Bloch equations [21,22]. This value is notably high for such a steeply downward-dispersing metallic surface state on a metal substrate which has a large phase space for inelastic decay [23]. Topological surface states with a dispersion and spin structure similar to those of Rashba-split bands also show relatively long lifetimes [24], which is attributed to the reduction of phase space for decay due to spin conservation.

B. $m_j = 3/2$ bands above E_F

The higher-lying $p_x p_y$ ($m_j = 3/2$) surface bands shown schematically in Fig. 1(a) are excited by photon energies around 3.1 eV, generated by frequency doubling of the fundamental laser frequency. The results are shown in Fig. 3 on an energy scale for intermediate states [22]. The strongly dispersing features with the highest intensity shift upward with increasing photon energy. They are attributed to the initial states discussed in Sec. III A, as indicated by the dashed orange and green guides to the eye in Fig. 3 (taken from Fig. 2 and shifted by the pump photon energy). Deviations of these dashed curves from the experimental dispersion are due to the different bias voltages used in one- and monochromatic two-photon photoemission as described in Sec. II. The light-gray dashed curves mark the edges of the projected bulk band structure [see

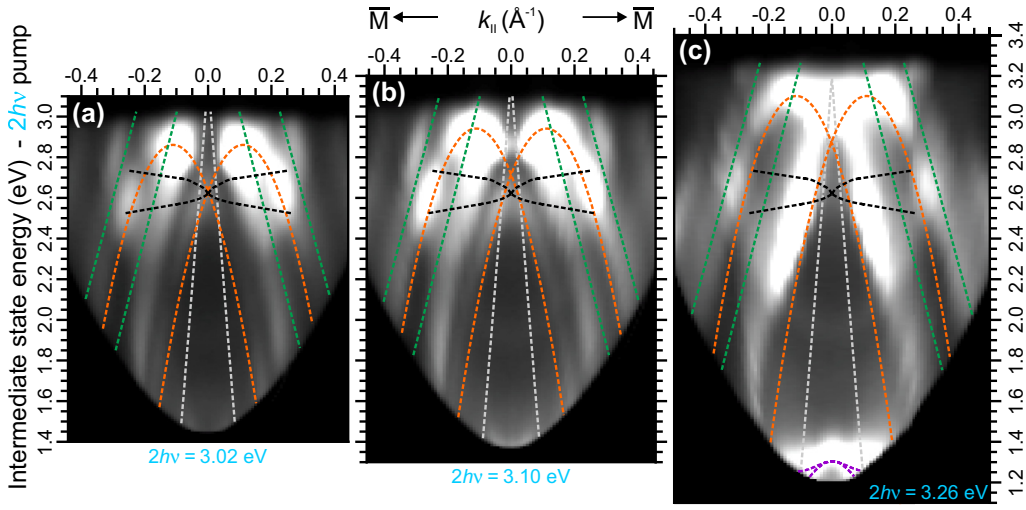

FIG. 3. Monochromatic two-photon photoemission data for three photon energies plotted on an intermediate-state energy scale. The dashed curves represent the edge of the projected bulk band structure (light gray, calculated based on Ref. [25]), the spin-split sp_z and $p_x p_y$ initial states (orange and green, taken from Fig. 2 and shifted by the pump photon energy), and the unoccupied p_z bands (black, extrapolated calculation of Ref. [8]). In (c) at the highest photon energy, the unoccupied $p_x p_y$ ($m_j = 3/2$) band rises above the photoemission horizon, as indicated by the dashed purple curve (calculation of Ref. [8]).

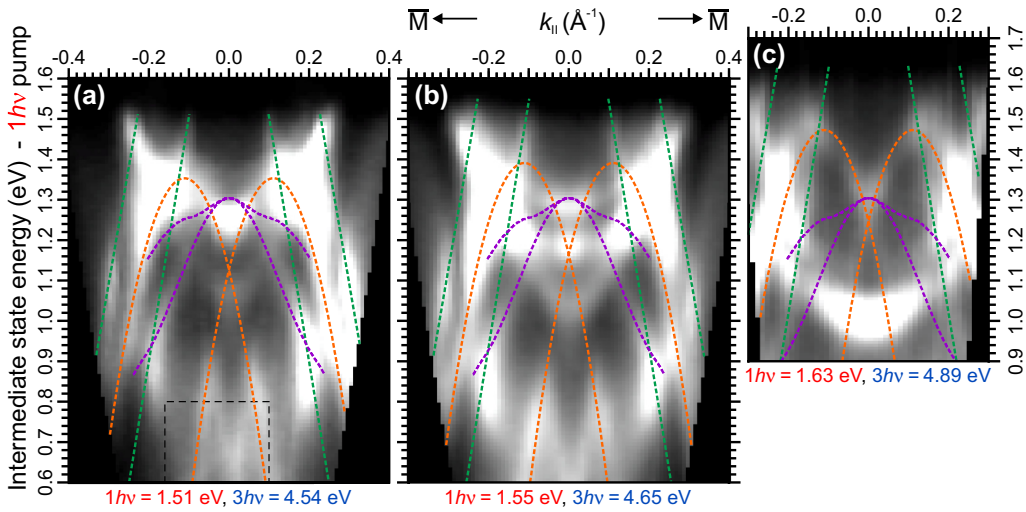

FIG. 4. Bichromatic two-photon photoemission data for three photon energies plotted on an energy scale for intermediate states pumped by the first harmonic. The dashed curves represent the spin-split sp_z and $p_x p_y$ initial states (orange and green, taken from Fig. 2 and shifted by the pump photon energy) as well as the unoccupied $p_x p_y$ ($m_j = 3/2$) bands (purple, calculation of Ref. [8]).

Fig. 1(a)] as calculated using the band structure parameters of Ref. [25]. Within the band gap, high intensity is observed around 1.3 eV at the highest accessible photon energy of 3.26 eV, as indicated by the dashed purple curve in Fig. 3(c). For lower photon energies these intermediate-state electrons cannot overcome the vacuum barrier in the second excitation step. This intensity is assigned to the $p_x p_y$ ($m_j = 3/2$) bands shown in Fig. 1(a).

The intensity maps shown in Fig. 3 change considerably with photon energy within the limited range from 3.02 to 3.26 eV. In addition to the initial states discussed before, a feature around 2.6 eV intermediate-state energy and parallel momentum of ± 0.3 Å^{-1} can be identified. It is assigned to the unoccupied p_z bands shown in Fig. 1(a). The dashed black curves represent the calculated dispersion of Ref. [8] (linearly extrapolated for $|k_{\parallel}| > 0.15$ Å^{-1} and shifted in energy to match the experimental data). Note that this state also appears with weaker intensity around zero parallel momentum for the lower photon energies, while it appears with high intensity when it is resonantly excited from the occupied sp_z or $p_x p_y$ ($m_j = 1/2$) bands. For p-polarized light sp_z to p_z transitions are allowed from dipole selection rules [26] and usually have higher intensity than the excitation from p_x (or p_y) initial states by the component of the electric field vector parallel to the surface. Note that the above-discussed $p_x p_y$ ($m_j = 3/2$) and p_z bands are also spin split, albeit not with a Rashba-type dispersion [8].

Resonant transitions between initial and intermediate states are also observed in the bichromatic two-photon photoemission maps in Fig. 4 [22]. The data are plotted on an energy scale applicable for intermediate states pumped by the fundamental of the laser. The dashed rectangle in Fig. 4(a) marks the region of the $p_x p_y$ ($m_j = 1/2$) bands discussed in Sec. III A. The lower pump and higher probe photon energy should allow us to map the dispersion of the $p_x p_y$ ($m_j = 3/2$) band whose maximum appeared in Fig. 3(c). The dashed purple curves in Fig. 4 represent the calculated dispersion of Ref. [8]. They match the experiment near zero parallel momentum, consistent with the monochromatic data of Fig. 3(c). The agreement is also fair for the lower branch, which steeply disperses between 0.9 and 1.3 eV and ± 0.2 Å^{-1}. However, a full dispersion cannot be readily extracted from the experimental data due to the strongly changing intensities even over the limited range of pump photon energies from 1.51 to 1.63 eV. We note that the dispersions of the initial states represented by the dashed orange and green guides to the eye (taken from Fig. 2 and shifted by the pump photon energy) coincide rather well with the various intensity enhancements observed at finite parallel momenta. The latter point towards resonant transitions into intermediate states other than the $p_x p_y$ ($m_j = 3/2$) band. However, no other unoccupied surface states are present in the energy window pumped by the first harmonic [see Fig. 1(a)]. The highly complex bichromatic two-photon photoemission patterns in Fig. 4 will be further disentangled in Sec. III C.

C. Image-potential states

The preceding section showed that the bichromatic two-photon photoemission data cannot be explained exclusively by the initial states or intermediate states pumped by the fundamental of the laser. This leads to the conclusion that some of the observed transitions correspond to intermediate states pumped by the third harmonic of the laser. Figure 5 shows the data on the appropriate energy scale. The intensity maps for the two lower photon energies [see Figs. 4(a) and 4(b)] are overlaid in red and green in Fig. 5(a). In this way the parabolic dispersion of the multiple resonances between 3.8 and 4.2 eV intermediate-state energy becomes evident. Note in particular that the intensity strongly changes with photon energy, and the individual resonances occur at slightly different energies and momenta due to resonant transitions from the steep initial bands. The dashed yellow fit curve indicates the corresponding parabolic band with the energy minimum at 3.8 eV. The effective mass of the parabolic band is 1.09 ± 0.06 times the free-electron mass m_e, and the binding energy relative to the vacuum level E_{vac} is around 0.7 eV. Such values are characteristic for image-potential states [15,16], and

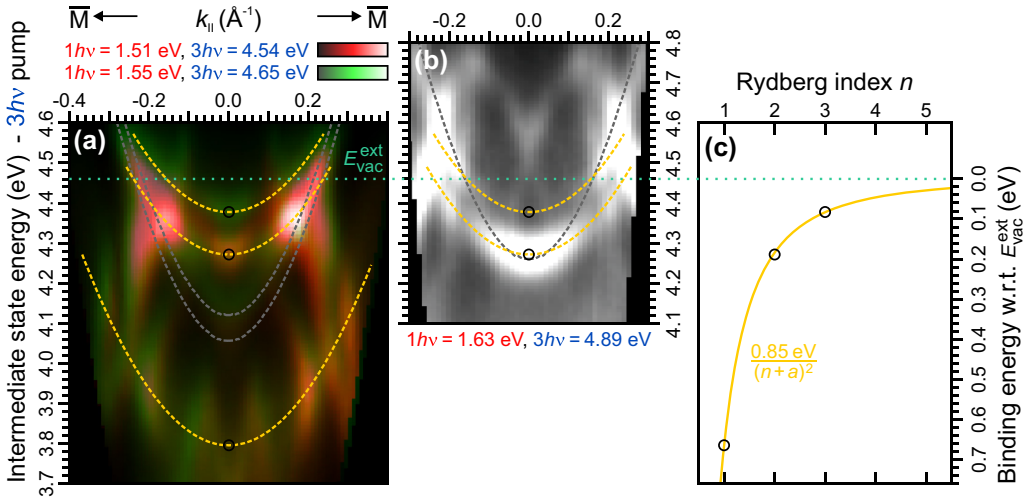

FIG. 5. (a) Bichromatic two-photon photoemission data for the two-photon energies from Figs. 4(a) and 4(b) overlaid on an energy scale relative for intermediate states pumped by the third harmonic. (b) Data from Fig. 4(c) for pump photon energy of 4.89 eV. (c) Binding energy of the first three image-potential states relative to the extrapolated vacuum level and fit to the quantum defect model. The dashed yellow (fits to data) and gray (calculated based on Ref. [25]) curves represent the image-potential states and direct bulk transitions, respectively.

we therefore identify the above feature as the first ($n = 1$) member of the corresponding Rydberg-type series. Indeed, the next two members, $n = 2$, 3, of the series of image-potential states can be identified at higher energies via parabolic fits to the data of Figs. 5(a) and 5(b). Note that, strictly speaking, all of these bands are image-potential resonances as the bulk band gap closes at around 3 eV above E_F [8] [see Figs. 1(a) and 3].

The Rydberg series can be fitted well by the quantum defect model $E^{ext}_{vac} - E_n = 0.85\,\text{eV}/(n+a)^2$ [27] with a quantum defect of $a = 0.128 \pm 0.005$ and an extrapolated vacuum level $E^{ext}_{vac} = 4.464 \pm 0.004$ eV. With respect to E^{ext}_{vac} the binding energies of the three resonances are obtained as 0.66, 0.19, and 0.08 eV, as shown in Fig. 5(c). The extrapolated vacuum level represents the local work function of Bi/Ag(111) and therefore is a more appropriate binding-energy reference than the previously determined work function of 4.49 eV (see Sec. II). Since the determination via the low-energy spectral cutoff in monochromatic two-photon photoemission averages over the sample surface [28], the higher value compared to E^{ext}_{vac} may be attributed to remaining regions of pristine Ag(111), which has a higher work function than Bi/Ag(111) [17]. An inverse photoemission study for Bi/Ag(111) reported a binding energy for the first image-potential state of 0.74 eV using a work function of 4.57 eV [29]. Referring to our vacuum level as extracted from the Rydberg series, the binding energy would be 0.63 eV, which is very close to our value of 0.66 eV. For image-potential states near the upper band edge of the projected bulk band structure a quantum defect $a = 0$ is expected [16,27]. This holds for a bulk-terminated crystal surface, but the $BiAg_2$ layer adds an additional phase shift to the wave function [30]. Following the model of Ref. [31], we obtain a phase shift for the $n = 1$ image-potential state of 0.86π, which is considerably larger than for monolayer graphene on noble-metal surfaces [31]. More interesting is the fact that for the $n = 1$ image-potential state on Bi/Ag(111) the total phase shift amounts to 4π compared to 2π for graphene monolayers. This agrees with the existence of two totally symmetric surface states (sp_z and p_z) below the first image-potential state for Bi/Ag(111), in contrast to one Shockley-type surface state for noble-metal surfaces (with or without graphene on top).

The complex patterns obtained in bichromatic two-photon photoemission involve occupied and unoccupied Rashba bands as well as image-potential states and resonant transitions between them. Further contributions might come from direct optical transitions between free-electron-like bulk bands induced by the third harmonic at photon energies between 4.5 and 4.9 eV. The excited electrons are then emitted by the second photon from the fundamental laser radiation. Such transitions can also be observed on the clean Ag(111) surface, where they appear with intensities comparable to those of the image-potential bands [32]. They can be distinguished from the latter due to the stronger dispersion corresponding to a smaller effective mass. The gray dashed curves in Figs. 5(a) and 5(b) represent these transitions as calculated using the band structure parameters of Ref. [25] and taking into account the different photon energies. They might well add to the observed intensity in the respective regions. In this context we note that the direct transition between bulk bands and the occupied sp_z and $p_x p_y$ Rashba bands have comparable intensities in the photoemission data of the bottom part of Fig. 2.

D. Circular dichroism

In Rashba bands states with opposite parallel momentum have opposite spin orientation. In the presence of spin-orbit coupling the relative spin orientation may be accessed in photoemission using circularly polarized light [33,34]. In our experiments at low photon energies the final states are in an energy range where only one free-electron-like band of predominantly s character exists in the silver band structure [35] which couples to one outgoing plane wave in vacuum. Therefore, the final-state bands have negligible spin-orbit coupling, and complications with sign reversals of the circular dichroism known for higher photon energies can be excluded

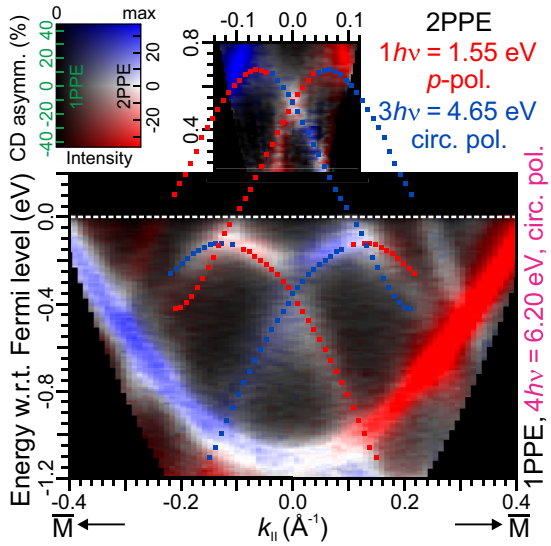

FIG. 6. Circular dichroism for the $p_x p_y$ ($m_j = 1/2$) bands above E_F complemented by the corresponding data for the occupied bands (see Fig. 2). The circular dichroism signal is overlaid in a color code on the summed spectra for right- and left-circularly polarized light. The contrast is chosen differently for the upper and lower parts to enhance the visibility of the weak dichroism asymmetry of the unoccupied $p_x p_y$ bands. The red and blue squares indicate the sign of the spin projection onto an axis perpendicular to $k_\parallel$ and the surface normal (calculation of Ref. [8], scaled and shifted to match the experimental dispersion).

[14,36]. The bottom part of Fig. 6 shows circular dichroism data taken with 6.20 eV photon energy for the sp_z Rashba bands. The direct transition between the nearly-free-electron-like bulk bands (see Fig. 2) also shows a strong dichroism of up to ±45%. This is explained by the fact that the electrons are not emitted in the mirror plane. In this situation electronic states of opposite parallel momenta are not equivalent in the bulk. Electrons still have opposite spin but also have opposite group velocities [37]. The dichroism stems from the initial states, which are free-electron-like bands of predominantly p_z character [35].

The occupied sp_z bands show a dichroism of up to 20% and opposite signs for the two branches, as well as sign reversals at the band maxima. This is in agreement with the calculated spin structure [8]. However, the sign reversal at the band maxima is not observed in photoemission results for Bi on a 20-monolayer Ag film [34]. This study used 22 eV photons in an energy range where rapid sign changes of the spin polarization with photon energy and parallel momentum have been reported [14].

The unoccupied $p_x p_y$ ($m_j = 1/2$) bands in the top part of Fig. 6 display a weak circular dichroism of ±10%. The sign is opposite to that of the occupied sp_z bands. Near the band maxima, apparently, no sign reversal is observed. However, the dichroism signal of ±25% in this region should not be attributed to the unoccupied $p_x p_y$ bands (see Fig. 2 and Sec. III A) and is most likely from near-resonant transitions from the occupied sp_z bands, as indicated in Fig. 1(a). If we follow the outer branches of the $p_x p_y$ bands below E_F, we observe the opposite sign of the dichroism compared to that of the inner branches above E_F, in agreement with the calculated spin structure [8] and the occupied sp_z bands. A spin-polarized inverse photoemission study complemented by calculations within a one-step model [12] found no sign reversal at the band maxima of the unoccupied $p_x p_y$ bands, in contrast to our findings. This might be attributed to the influence of the orbital symmetry of the respective states in combination with the experimental geometry.

For the monochromatic two-photon photoemission data of Fig. 3 no circular dichroism measurements were performed because the polarization of pump and probe photons of the same energy could not be controlled independently. Since the data are dominated by initial-state effects, the obtainable information is expected to be similar to that in Fig. 6 (bottom). In the region where resonant transitions from the occupied states via the unoccupied p_z band take place, some interesting effects might occur.

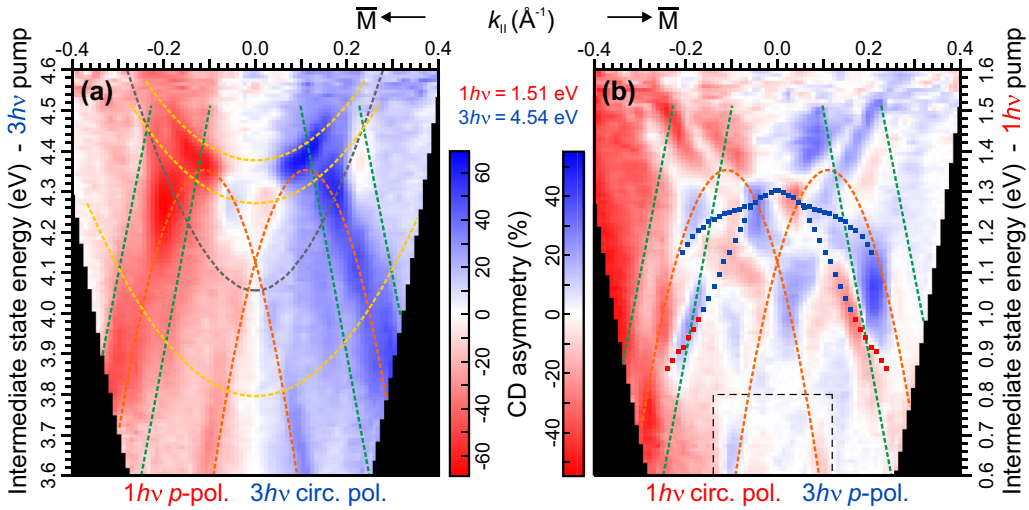

FIG. 7. Circular dichroism in a color code for the (a) image-potential states and (b) $p_x p_y$ ($m_j = 3/2$) bands above E_F, taken with photon energy $1h\nu = 1.51$ eV [see Figs. 5(a) and 4(a), respectively]. In (a) the third harmonic is circularly polarized, whereas (b) was recorded for the circularly polarized fundamental. The dashed curves retain their assignments from Figs. 4 and 5. The red and blue squares in (b) indicate the sign of the spin projection onto an axis perpendicular to $k_\parallel$ and the surface normal for the $p_x p_y$ ($m_j = 3/2$) bands (calculation of Ref. [8]).

Such resonant transitions have been observed in the bichromatic measurements in Figs. 4 and 5. The corresponding circular dichroism data are shown in Fig. 7 and exhibit drastic differences depending on which photon is circularly polarized. Figure 7(a) shows the case when the third harmonic is circularly polarized, and Fig. 7(b) shows the case for the circularly polarized fundamental. The data are plotted on an energy scale corresponding to the intermediate states pumped by the circularly polarized light. The p-polarized probe then samples the asymmetry in the population of the intermediate states induced by the circularly polarized pump photons of opposite helicity. The asymmetry might arise from the initial or intermediate states or both.

In Fig. 7(a) the intermediate states pumped by the circularly polarized third harmonic are image-potential states. They are unpolarized or, more precisely, have a Rashba splitting [38] not resolvable with our energy and momentum resolution. The circular dichroism should then be dominated by the initial states. The main dichroism asymmetry of up to $\pm 60\%$ indeed follows the occupied sp_z bands (with opposite sign), similar to the bottom part of Fig. 6. We note that the dichroism in Fig. 7(a) is largely dominated by a right/left asymmetry. This most likely stems from the asymmetry of the bulk bands which contribute initial states outside the band gap of the projected bulk band structure. The occupied $p_x p_y$ bands seem to provide no strong dichroism contrast in spite of the fact that resonant transitions via image-potential states are observed (see Fig. 4).

In Fig. 7(b) the circularly polarized fundamental pumps intermediate states from the spin-split Rashba manifold, in particular the $p_x p_y$ bands. The unoccupied part of the lower $m_j = 1/2$ bands is located in the area of the dashed rectangle and was already presented and discussed in the context of Fig. 6. The unoccupied $m_j = 3/2$ bands overlap with the initial states, and the dichroism patterns appear rich in structure. Note that a clear circular dichroism contrast of up to $\pm 25\%$ is observed where the $m_j = 3/2$ bands cross the initial states in spite of the fact that no strong resonances between these bands were seen in the intensity maps in Fig. 4. On the other hand, pronounced resonant transitions occur via the image-potential states which have negligible Rashba splitting. However, the image-potential states show up in the dichroism pattern with asymmetries of up to $\pm 30\%$, as can be seen for the $n = 2$ and 3 bands in the top part of Fig. 7(b). The sign of the dichroism follows the right/left asymmetry from Fig. 7(a) and the outer parts of Fig. 7(b). We therefore attribute this dichroism to the bulk bands serving as initial states in these regions. Finally, we would like to point out that the circular dichroism in some cases provides a clearer picture of the bands than the intensity distributions dominated by resonant transitions.

TABLE I. Energies at $k_\parallel = 0$, effective masses m^* ($\pm 0.06 m_e$) and Rashba parameters α_R of the observed states. Energies are given relative to E_F for the spin-split bands and as binding energies relative to E_{vac}^{ext} for the image-potential states n.

State	m_j	Energy (eV)	Literature	m^* (units of m_e)	α_R (eV Å)
sp_z		-0.36 ± 0.02	-0.33 [10]	-0.33	3.04 ± 0.08
$p_x p_y$	1/2	0.53 ± 0.02	0.55 [10]	-0.16	3.0 ± 0.2
$p_x p_y$	3/2	1.30 ± 0.02	1.2 [12]		
p_z		2.60 ± 0.06	2.6 [12]		
$n = 1$		0.66 ± 0.02	0.74 [29]	1.09	
$n = 2$		0.19 ± 0.02		1.14	
$n = 3$		0.08 ± 0.04		1.12	

IV. SUMMARY AND CONCLUSIONS

The data for the observed states at the center of the surface Brillouin zone (parallel momentum $k_\parallel = 0$) are compiled in Table I. The agreement with results from scanning tunneling spectroscopy [10] and inverse photoemission [12,29] is excellent. Note that calculations give similar values for the $p_x p_y$ bands and slightly varying values for the p_z bands [8,12], presumably because the latter are more sensitive to the outward relaxation of the bismuth atoms within the top $BiAg_2$ layer.

The analysis of the two-photon photoemission spectra is complicated by resonant transitions between the various Rashba and image-potential bands. Using different photon energies, we succeeded in disentangling the highly complex two-photon photoemission maps recorded in the $\overline{\Gamma M}$ direction. Circular dichroism proved the expected Rashba-type spin structure of the lower sp_z and $p_x p_y$ ($m_j = 1/2$) bands, in agreement with theoretical predictions [8]. For the higher $p_x p_y$ ($m_j = 3/2$) and image-potential bands the circular dichroism patterns become quite rich in structure. However, they reveal additional information beyond the intensity maps dominated by resonant transitions. It would be desirable to extend the studies to the $\overline{\Gamma K}$ direction to avoid the circular dichroism asymmetry originating from the bulk bands.

[1] E. I. Rashba, Spin-orbit coupling goes global, J. Phys.: Condens. Matter **28**, 421004 (2016).

[2] D. Hsieh, Y. Xia, D. Qian, L. Wray, J. H. Dil, F. Meier, J. Osterwalder, L. Patthey, J. G. Checkelsky, N. P. Ong, A. V. Fedorov, H. Lin, A. Bansil, D. Grauer, Y. S. Hor, R. J. Cava, and M. Z. Hasan, A tunable topological insulator in the spin helical dirac transport regime, Nature (London) **460**, 1101 (2009).

[3] E. I. Rashba, Properties of semiconductors with an extremum loop. 1. Cyclotron and combinational resonance in a magnetic field perpendicular to the plane of the loop, Sov. Phys. Solid State **2**, 1109 (1960).

[4] Yu. A. Bychkov and E. I. Rashba, Oscillatory effects and the magnetic susceptibility of carriers in inversion layers, J. Phys. C **17**, 6039 (1984).

[5] C. R. Ast, J. Henk, A. Ernst, L. Moreschini, M. C. Falub, D. Pacilé, P. Bruno, K. Kern, and M. Grioni, Giant Spin Splitting through Surface Alloying, Phys. Rev. Lett. **98**, 186807 (2007).

[6] M. Liebmann, C. Rinaldi, D. Di Sante, J. Kellner, C. Pauly, R. N. Wang, J. E. Boschker, A. Giussani, S. Bertoli, M. Cantoni, L. Baldrati, M. Asa, I. Vobornik, G. Panaccione, D. Marchenko, J. Sánchez-Barriga, O. Rader, R. Calarco, S. Picozzi, R. Bertacco,

and M. Morgenstern, Giant Rashba-Type Spin Splitting in Ferroelectric GeTe(111), Adv. Mater. **28**, 560 (2016).

[7] D. Niesner, M. Wilhelm, I. Levchuk, A. Osvet, S. Shrestha, M. Batentschuk, C. Brabec, and Th. Fauster, Giant Rashba Splitting in $CH_3NH_3PbBr_3$ Organic-Inorganic Perovskite, Phys. Rev. Lett. **117**, 126401 (2016).

[8] G. Bihlmayer, S. Blügel, and E. V. Chulkov, Enhanced Rashba spin-orbit splitting in BiAg(111) and PbAg(111) surface alloys from first principles, Phys. Rev. B **75**, 195414 (2007).

[9] I. M. McLeod, V. R. Dhanak, A. Matilainen, M. Lahti, K. Pussi, and K. H. L. Zhang, Structure determination of the $p(\sqrt{3} \times \sqrt{3})R30^\circ$ BiAg(111) surface alloy using LEED IV and DFT analyses, Surf. Sci. **604**, 1395 (2010).

[10] L. El-Kareh, P. Sessi, T. Bathon, and M. Bode, Quantum Interference Mapping of Rashba-Split Bloch States in Bi/Ag(111), Phys. Rev. Lett. **110**, 176803 (2013).

[11] S. Schirone, E. E. Krasovskii, G. Bihlmayer, R. Piquerel, P. Gambardella, and A. Mugarza, Spin-Flip and Element-Sensitive Electron Scattering in the $BiAg_2$ Surface Alloy, Phys. Rev. Lett. **114**, 166801 (2015).

[12] S. N. P. Wissing, A. B. Schmidt, H. Mirhosseini, J. Henk, C. R. Ast, and M. Donath, Ambiguity of Experimental Spin Information from States with Mixed Orbital Symmetries, Phys. Rev. Lett. **113**, 116402 (2014).

[13] R. Noguchi, K. Kuroda, K. Yaji, K. Kobayashi, M. Sakano, A. Harasawa, T. Kondo, F. Komori, and S. Shin, Direct mapping of spin and orbital entangled wave functions under interband spin-orbit coupling of giant Rashba spin-split surface states, Phys. Rev. B **95**, 041111 (2017).

[14] H. Bentmann, H. Maaß, E. E. Krasovskii, T. R. F. Peixoto, C. Seibel, M. Leandersson, T. Balasubramanian, and F. Reinert, Strong Linear Dichroism in Spin-Polarized Photoemission from Spin-Orbit-Coupled Surface States, Phys. Rev. Lett. **119**, 106401 (2017).

[15] K. Giesen, F. Hage, F. J. Himpsel, H. J. Riess, and W. Steinmann, Two-Photon Photoemission via Image-Potential States, Phys. Rev. Lett. **55**, 300 (1985).

[16] U. Höfer and P. M. Echenique, Resolubility of image-potential resonances, Surf. Sci. **643**, 203 (2016).

[17] K. H. L. Zhang, I. M. McLeod, M. Lahti, K. Pussi, and V. R. Dhanak, The evolution of the electronic structure at the Bi/Ag(111) interface studied using photoemission spectroscopy, J. Phys.: Condens. Matter **24**, 435502 (2012).

[18] M. Hengsberger, F. Baumberger, H. J. Neff, T. Greber, and J. Osterwalder, Photoemission momentum mapping and wave function analysis of surface and bulk states on flat Cu(111) and stepped Cu(443) surfaces: A two-photon photoemission study, Phys. Rev. B **77**, 085425 (2008).

[19] S. Pawlik, R. Burgermeister, M. Bauer, and M. Aeschlimann, Direct transition in the system Ag(111) studied by one- and two-photon photoemission, Surf. Sci. **402–404**, 556 (1998).

[20] A. Winkelmann, V. Sametoglu, J. Zhao, A. Kubo, and H. Petek, Angle-dependent study of a direct optical transition in the *sp* bands of Ag(111) by one- and two-photon photoemission, Phys. Rev. B **76**, 195428 (2007).

[21] K. Boger, M. Roth, M. Weinelt, Th. Fauster, and P.-G. Reinhard, Linewidths in energy-resolved two-photon photoemission spectroscopy, Phys. Rev. B **65**, 075104 (2002).

[22] See Supplemental Material at http://link.aps.org/supplemental/10.1103/PhysRevB.98.085430 for the fits of the time-resolved spectra and the raw data of the energy distribution curves.

[23] K. Boger, M. Weinelt, and Th. Fauster, Scattering of Hot Electrons by Adatoms at Metal Surfaces, Phys. Rev. Lett. **92**, 126803 (2004).

[24] D. Niesner, S. Otto, Th. Fauster, E. V. Chulkov, S. V. Eremeev, O. E. Tereshchenko, and K. A. Kokh, Electron dynamics of unoccupied states in topological insulators, J. Electron Spectrosc. Relat. Phenom. **195**, 258 (2014).

[25] D. A. Papaconstantopoulos, *Handbook of the Band Structure of Elemental Solids* (Plenum, New York, 1986).

[26] W. Eberhardt and F. J. Himpsel, Dipole selection rules for optical transitions in the fcc and bcc lattices, Phys. Rev. B **21**, 5572 (1980).

[27] Th. Fauster and W. Steinmann, Two-photon photoemission spectroscopy of image states, in *Photonic Probes of Surfaces*, edited by P. Halevi, Electromagnetic Waves: Recent Developments in Research (North-Holland, Amsterdam, 1995), Vol. 2, Chap. 8, p. 347.

[28] R. Fischer, S. Schuppler, N. Fischer, Th. Fauster, and W. Steinmann, Image States and Local Work Function for Ag/Pd(111), Phys. Rev. Lett. **70**, 654 (1993).

[29] S. N. P. Wissing, Heavy elements on noble metal surfaces: Spin effects in the unoccupied states, Ph.D. thesis, Universität Münster, 2015.

[30] R. Fischer and Th. Fauster, Coupling of image states to quantum-well states for Au on Pd(111), Phys. Rev. B **51**, 7112 (1995).

[31] D. Nobis, M. Potenz, D. Niesner, and Th. Fauster, Image-potential states of graphene on noble-metal surfaces, Phys. Rev. B **88**, 195435 (2013).

[32] M. Marks, C. H. Schwalb, K. Schubert, J. Güdde, and U. Höfer, Quantum-beat spectroscopy of image-potential resonances, Phys. Rev. B **84**, 245402 (2011).

[33] G. Bian, L. Zhang, Y. Liu, T. Miller, and T.-C. Chiang, Illuminating the Surface Spin Texture of the Giant-Rashba Quantum-Well System Bi/Ag(111) by Circularly Polarized Photoemission, Phys. Rev. Lett. **108**, 186403 (2012).

[34] B. Guang, T. Miller, and T.-C. Chiang, Rashba splitting and dichroism of surface states in Bi/Ag surface alloy, J. Electron Spectrosc. Relat. Phenom. **201**, 36 (2015).

[35] N. V. Smith, Phase analysis of image states and surface states associated with nearly-free-electron band gaps, Phys. Rev. B **32**, 3549 (1985).

[36] M. R. Scholz, J. Sánchez-Barriga, J. Braun, D. Marchenko, A. Varykhalov, M. Lindroos, Y. J. Wang, H. Lin, A. Bansil, J. Minár, H. Ebert, A. Volykhov, L. V. Yashina, and O. Rader, Reversal of the Circular Dichroism in Angle-Resolved Photoemission from Bi_2Te_3, Phys. Rev. Lett. **110**, 216801 (2013).

[37] J. Kanasaki, H. Tanimura, K. Tanimura, Ph. Ries, W. Heckel, K. Biedermann, and Th. Fauster, Ultrafast dynamics in photoexcited valence-band states of Si studied by time- and angle-resolved photoemission spectroscopy of bulk direct transitions, Phys. Rev. B **97**, 035201 (2018).

[38] T. Nakazawa, N. Takagi, M. Kawai, H. Ishida, and R. Arafune, Rashba splitting in an image potential state investigated by circular dichroism two-photon photoemission spectroscopy, Phys. Rev. B **94**, 115412 (2016).